SPACE WEATHER, VOL. 8, S00E02, doi:10.1029/2009SW000523, 2010

Click Here for Full Article

Earth-Moon-Mars Radiation Environment Module framework

N. A. Schwadron,[1] L. Townsend,[2] K. Kozarev,[1] M. A. Dayeh,[3] F. Cucinotta,[4] M. Desai,[3] M. Golightly,[1] D. Hassler,[5] R. Hatcher,[2] M.-Y. Kim,[4] A. Posner,[6] M. PourArsalan,[2] H. E. Spence,[1] and R. K. Squier[7]

Received 6 September 2009; revised 22 October 2009; accepted 26 October 2009; published 9 January 2010.

[1] We are preparing to return humans to the Moon and setting the stage for exploration to Mars and beyond. However, it is unclear if long missions outside of low-Earth orbit can be accomplished with acceptable risk. The central objective of a new modeling project, the Earth-Moon-Mars Radiation Exposure Module (EMMREM), is to develop and validate a numerical module for characterizing time-dependent radiation exposure in the Earth-Moon-Mars and interplanetary space environments. EMMREM is being designed for broad use by researchers to predict radiation exposure by integrating over almost any incident particle distribution from interplanetary space. We detail here the overall structure of the EMMREM module and study the dose histories of the 2003 Halloween storm event and a June 2004 event. We show both the event histories measured at 1 AU and the evolution of these events at observer locations beyond 1 AU. The results are compared to observations at Ulysses. The model allows us to predict how the radiation environment evolves with radial distance from the Sun. The model comparison also suggests areas in which our understanding of the physics of particle propagation and energization needs to be improved to better forecast the radiation environment. Thus, we introduce the suite of EMMREM tools, which will be used to improve risk assessment models so that future human exploration missions can be adequately planned for.

Citation: Schwadron, N. A., et al. (2010), Earth-Moon-Mars Radiation Environment Module framework, *Space Weather*, *8*, S00E02, doi:10.1029/2009SW000523.

1. Introduction

[2] The hazards posed by particle radiation in space depicted in Figure 1 pose a serious challenge to human and robotic exploration missions to the Moon, Mars and beyond. The hazards include the following.

[3] 1. Galactic cosmic rays (GCRs), which are always present in the near Earth space environment and throughout the solar system, originate from beyond our heliosphere and produce chronic but not acute exposures. GCRs are very difficult to shield against beyond the Earth's protective atmosphere and magnetosphere. Astronauts under typical shielding of a few g/cm^2 of aluminum could reach their career limit of radiation exposure from GCRs in roughly 3 years [*Cucinotta et al.*, 2001]. Current research in this area is focused on understanding the constraints imposed by GCRs and how they vary with mission transit time, shielding type and thickness, and on developing better techniques to shield against GCRs. The intensities of GCRs vary with the solar cycle with the largest intensities occurring near solar minimum when interplanetary field strengths [e.g., *Le Roux and Potgieter*, 1995] are weakest and there are the fewest number of interplanetary disturbances from transient disturbances such as coronal mass ejections [e.g., *Owens and Crooker*, 2006; *Schwadron et al.*, 2008]. GCRs are modulated by the outflowing solar wind and its embedded magnetic field; the modulation is therefore weakest when the interplanetary field strength is low [e.g., *Potgieter et al.*, 2001] and the associated intensities of GCRs are commensurately high.

[1]Department of Astronomy, Boston University, Boston, Massachusetts, USA.
[2]Department of Nuclear Engineering, University of Tennessee, Knoxville, Tennessee, USA.
[3]Southwest Research Institute, San Antonio, Texas, USA.
[4]Johnson Space Center, NASA, Houston, Texas, USA.
[5]Space Studies Department, Southwest Research Institute, Boulder, Colorado, USA.
[6]NASA Headquarters, Washington, D. C., USA.
[7]Computer Science Department, Georgetown University, Washington, D. C., USA.

Copyright 2010 by the American Geophysical Union

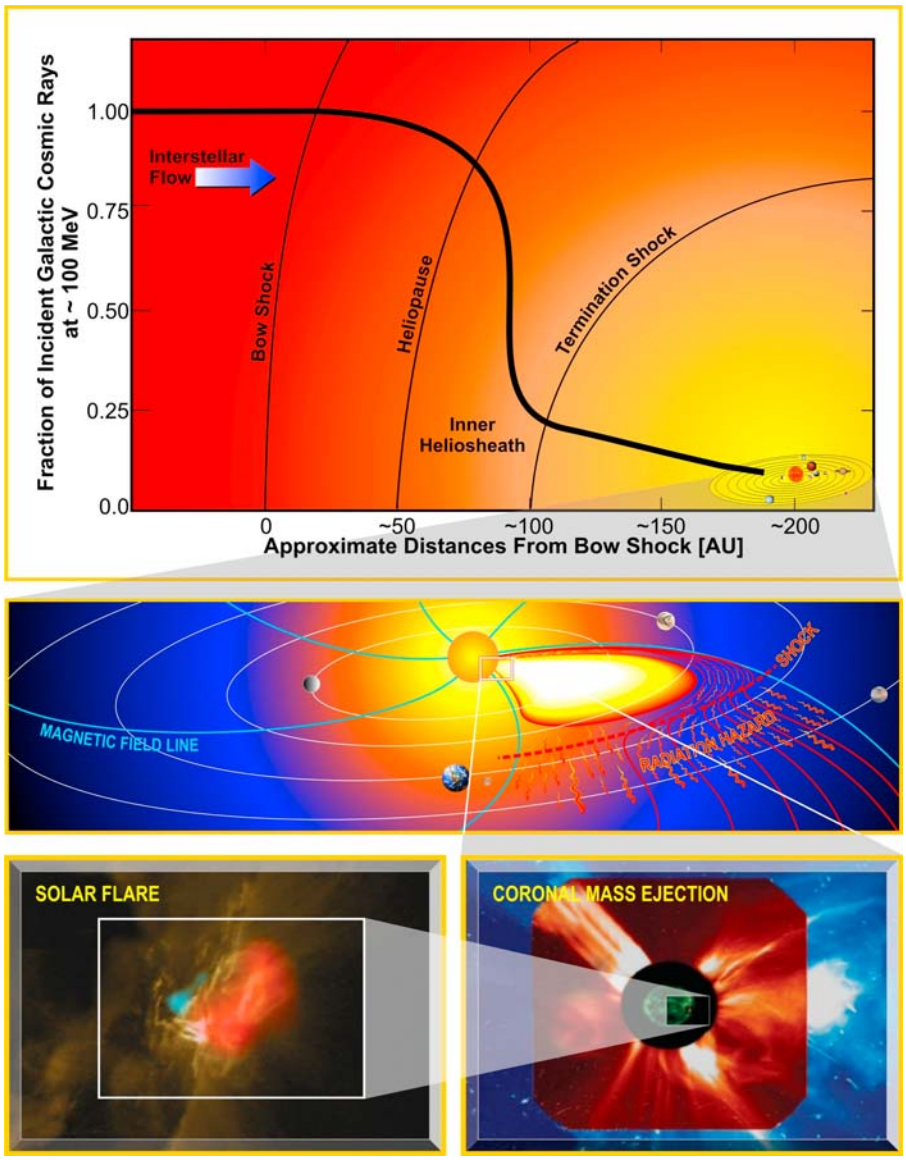

Figure 1. EMMREM provides a suite of numerical modules to characterize time-dependent radiation exposure from the hazards posed by space radiation: (top) galactic cosmic rays from outside our solar system and from (middle) shocks and (bottom left) flares often driven by (bottom right) coronal mass ejections.

[4] 2. Solar energetic particle (SEP) events (which we define to include ions; also solar particle events (SPEs)) are also dangerous to astronauts outside of Earth's protective layers (the atmosphere and magnetosphere). Current research in this area focuses on developing the ability to predict when and where SEP events will occur and finding ways to adequately shield against SEP-associated particle radiation.

[5] 3. There are unique radiation environments at each planet and their satellites. We have thoroughly characterized the locations of the radiation belts at Earth, which allows us to reduce the hazard they pose by rapidly transiting them. Human and robotic exploration of other planets and satellites requires that we adequately characterize planetary radiation environments and develop appropriate mitigation strategies and adequate shielding. Shielding is often considered the solution to space radiation hazards. Very high energy radiation (e.g., >100 MeV), however, produces secondary penetrating particles such as neutrons and nuclear fragments in shielding material. Some types of shielding material may actually increase the radiation hazard [*Wilson et al.*, 1999]. The radiation hazard

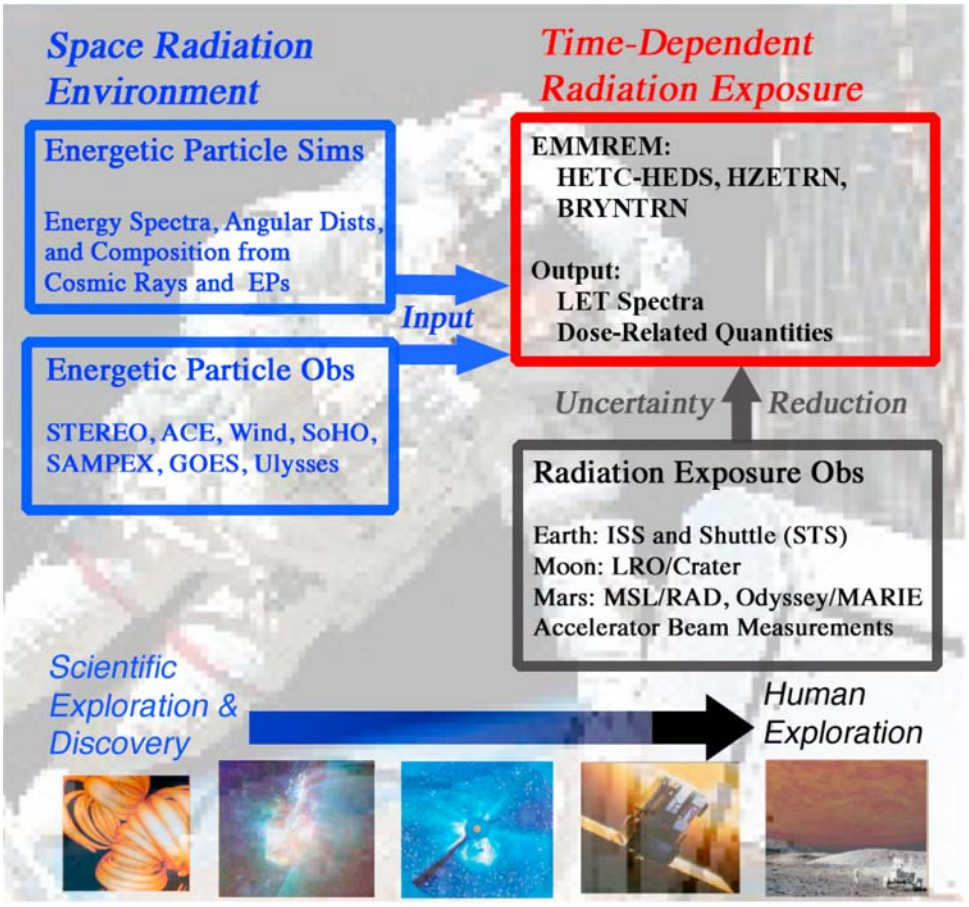

Figure 2. EMMREM provides an important link from the Space Science to Space Exploration programs by characterizing time-dependent radiation exposure from simulated and observed particle radiation events. The focus in EMMREM on validation studies provides a means for significant uncertainty reduction.

is not sufficiently well characterized to determine if long missions outside of low-Earth orbit can be accomplished with acceptable risk [*Cucinotta et al.*, 2001].

[6] Estimates of radiation hazards may be inaccurate through incomplete characterization in terms of net quantities such as accumulated dose. Time-dependent characterization often changes acute risk estimates [*Cucinotta*, 1999; *Cucinotta et al.*, 2000; *George et al.*, 2002]. Events with large accumulated doses but relatively low dose rates (<30 rad/h) pose significantly reduced risks. More complete characterization of radiation hazards requires that models take into account time-dependent radiation effects according to organ type, primary and secondary radiation composition, and acute effects (vomiting, sickness and, at high exposures, death) versus chronic effects (such as cancer). Further, to reduce uncertainties in predictions of radiation hazards, radiation exposure models should be tested with direct observations. This requires detailed knowledge of radiation detectors and accurate detector response models [*Nikjoo et al.*, 2002].

[7] We introduce here the Earth-Moon-Mars Radiation Environment Module (EMMREM), which is designed to predict the radiation environment at Earth, the Moon, Mars and throughout the interplanetary medium in the inner heliosphere. Section 2 describes the EMMREM project and the framework of modules associated with it. Section 3 describes EMMREM results applied to two recent SEP events. We highlight, in particular, areas of development required to improve radiation characterization and hazard prediction. Section 4 summarizes the article.

2. EMMREM Project and Framework

[8] Prediction of the radiation environment through the inner heliosphere requires an understanding of how evolving disturbances generate energetic particles, and how the energetic particles subsequently propagate and evolve through the inner heliosphere. There is a large effort in the space physics community to address these

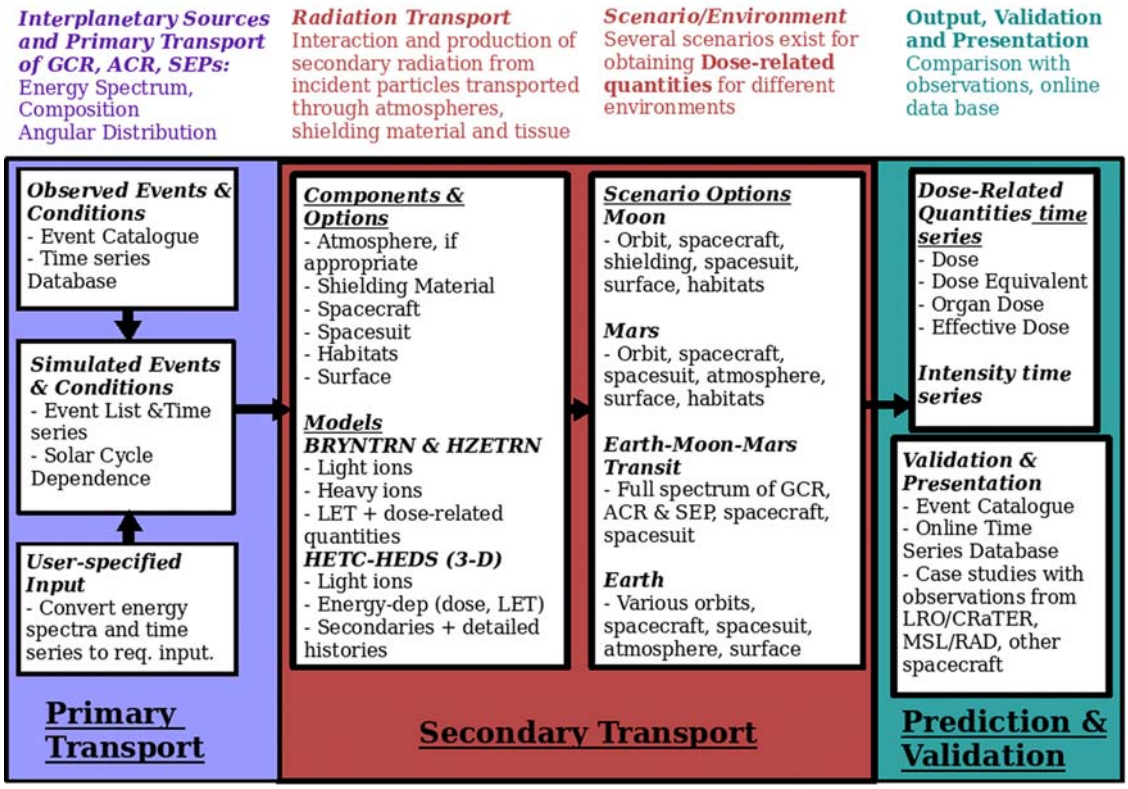

Figure 3. EMMREM provides a series of primary and secondary transport modules for the prediction and validation of particle radiation environment.

underlying questions. The central challenge in EMMREM is to develop flexible interfaces to the models and observations made in the space science community to assess the radiation environment.

[9] We have currently developed a first version of the EMMREM system, which consists of two primary pieces: The Energetic Particle Radiation Environment Module (EPREM) solves for the propagation and acceleration of energetic particles in the evolving magnetic fields of the inner heliosphere with input based on observations from satellites; the Baryon Transport Module (BRYNTRN) is a deterministic, coupled proton-neutron space radiation transport model that transports incident protons and their secondary products (protons, neutrons, deuterons, tritons, helions, and alphas) through shields of arbitrary composition and thickness [*Wilson et al.*, 1991]. EMMREM takes input based on solar energetic particle observations or simulations, propagates observed time series through the inner heliosphere, and derives the flux and dose time series at observers distributed throughout the inner heliosphere. The EMMREM framework is broken down based on the four pieces shown in Figure 2 and detailed in Figure 3.

[10] 1. The interplanetary source input provides the interplanetary energy spectrum, composition and angular distributions (SEPs, ACRs and GCRs) based on simulations, observed events and interplanetary conditions, or user-specified input. We are developing a database (available online) of simulated and observed events and time series.

[11] 2. The scenario/environment submodule transforms the interplanetary source energy spectra, composition and angular distributions based on shadowing by the planetary body, deflection/trapping by planetary magnetic fields, and propagation to different locations through the inner heliosphere. We are currently using the EPREM module for this purpose.

[12] 3. The radiation transport submodule describes the interaction of incident ionized particles with atmospheres, shielding material and tissue, including production of secondary forms of radiation including neutrons, protons and heavy ion recoil atoms, utilizing output from the Scenario submodule. We are currently using a combination of BRYNTRN for solar proton events (SPEs) and lookup tables to derive the doses from GCRs for this submodule.

[13] 4. EMMREM output includes time-dependent dose-related quantities. Events, time series, and case studies for validation are also collected into the online database.

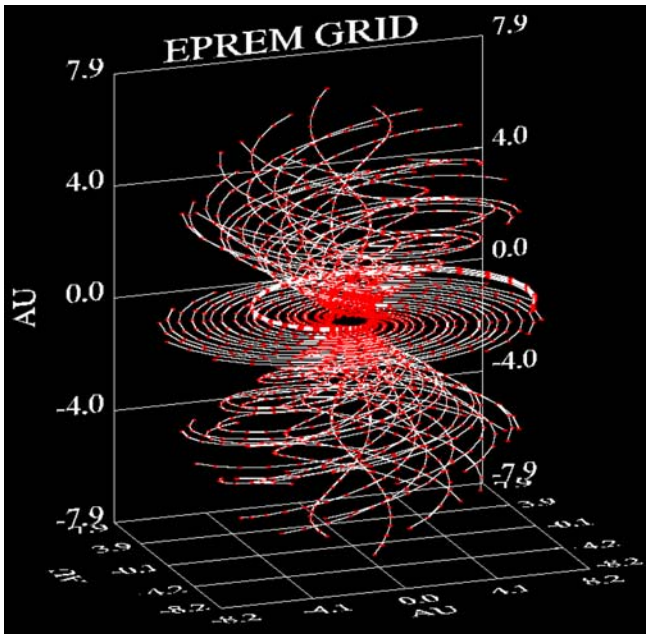

Figure 4. A three-dimensional system node is followed out with the evolving solar wind to solve the particle transport and acceleration equations in the Energetic Particle Radiation Environment Module. In the node mesh used here, we have focused on the ecliptic plane containing the Earth, the Moon, and Mars. The Ulysses spacecraft was also near the ecliptic plane during the observational periods studied in the paper.

2.1. Interplanetary Source Input

[14] We have identified candidate SEP events and will develop a detailed event catalog for solar cycle 23 (the current catalog contains 7 events). This catalog includes energetic particle, plasma, magnetic field, and flare data from different instruments (whenever available) on board the Advanced Composition Explorer (ACE) [*Stone et al.*, 1998], Solar Heliospheric Observatory (SOHO) [*Domingo et al.*, 1995], the Geostationary Operational Environmental Satellite (GOES) series, Mars Odyssey [*Saunders et al.*, 2001], and Ulysses [*Wenzel et al.*, 1992] spacecraft.

[15] For EPREM energetic particle input, we have obtained and verified proton data from GOES/SEM-EPS [*Sauer*, 1993] and SOHO/ERNE [*Torsti et al.*, 1995] over a broad energy range (1–500 MeV in case of GOES) at different time resolutions (1, 3, and 24 h) for all candidate events and provided data sets in a self-describing file format that is used in the EMMREM code. We have visualized the magnetic and radial alignment between the flare location and each spacecraft using ephemeris data. We have also developed a prioritized event list and data sets with relevant plasma and magnetic field quantities (speed, density, magnetic field) over a series of Carrington rotations.

[16] These SEP events and data sets will be made available for study online at the EMMREM Web site at BU and at the Community Coordinated Modeling Center (CCMC). In this paper, we show three examples of results from EMMREM event catalog. In addition to the EMMREM event catalogs, we are currently developing the capability to select arbitrary time series from the GOES database (http://www.swpc.noaa.gov/ftpmenu/lists/pchan.html). This capability will be available to users through the BU Web site and the CCMC.

2.2. Energetic Particle Radiation Environment Module

[17] EPREM traces individual nodes along magnetic field lines as they are carried out with the solar wind and solves the energetic particle transport equations in the comoving (Lagrangian) field aligned grid. Each grid node propagates out with the solar wind. In each time step Δt, a given node's displacement is simply $\Delta \mathbf{x} = \Delta t \mathbf{V}(\mathbf{x})$ where $\mathbf{x}$ is the grid location and $\mathbf{V}(\mathbf{x})$ is the solar wind velocity. A snapshot of this evolving node mesh is shown in Figure 4. On the inner boundary, grid nodes are spawned and rotated by angles consistent with the solar rotation rate at each time step. Grid nodes, like magnetic field lines, are frozen into the solar wind flow. Hence, the configuration of grid nodes naturally follows a Parker spiral field configuration.

[18] At each time step, a shell of nodes is spawned at the inner boundary, the inner boundary is rotated, and the nested shells of nodes (node shells) are advanced outward, radially away from the inner boundary. If the solar wind is uniform, the node shells lie on nested spherical surfaces. However, if the flow is nonuniform the nested surfaces of node shells become distorted (nonspherical). On each shell, the location of a given node is where a field line pierces the shell, and a list of nodes traced through nested shells follows a magnetic field line.

[19] We have also developed a special class of nodes that links up to a given observer (a location at a planet, moon or a satellite, where energetic particle distributions are projected). We refer to these as observer nodes, and the magnetic field lines attached to them as observer-connected field lines. One set of observer-connected field lines can be seen in Figure 4 looping up and around slightly above the ecliptic on the right-hand side of the image. This group of field lines connects to an observer near the position of the Ulysses spacecraft. The nodes along observer-connected field lines also migrate outward with the solar wind flow, but their angular positions are continually adjusted so that a given observer-connected field line passes through the given observer.

[20] The energetic particle solver is updated on the observer-connected field lines in the same manner as on normal evolving field lines. This presents some issues with the time histories of MHD quantities on observer-connected nodes. However, energetic particle propagation timescales are short compared to large-scale plasma evolution. The observer-connected field lines approximate the

conditions of energetic particle evolution as snapshots of the plasma conditions along the field line connected to the observer. Other mechanisms using interpolation of field lines near the observer were tried, but the proximity of nearest neighbor field lines varies with time introducing artificial temporal gradients in the predictions. The introduction of observer-connected field lines allows for much more accurate time histories.

[21] The grid has been set up to handle evolving flows. Interfaces have been constructed to both corotating MHD flow solutions (K. Kozarev et al., Streaming directionality and radiation effectiveness of a solar energetic proton event as modeled with the MHD-coupled EMMREM framework, manuscript in preparation, 2009) and to a new LFM-Helio MHD model under development by V. Merkin at Boston University (V. G. Merkin et al., LFM-helio: A new global heliosphere MHD model and initial results of coupling with EPREM, manuscript in preparation, 2009). In the simulations used in this paper, we assume a uniform solar wind flow, a density that falls off with the inverse square of radial distance from the Sun, and a nominal Parker spiral field configuration.

[22] Along each field line (a connected list of nodes) we solve for particle transport, adiabatic focusing, adiabatic cooling, convection, pitch angle scattering, and stochastic acceleration according to the formalism introduced recently [*Kóta et al.*, 2005]. A slightly modified form of the focused transport equation [*Skilling*, 1971; *Ruffolo*, 1995; *Tylka*, 2001; *Ng et al.*, 2003] is used to treat transport and energy change; however the coefficients are specified so they can be computed along nodes that move with the solar wind flow:

$$\left(1-\frac{\mathbf{V}\cdot\hat{e}_b v\mu}{c^2}\right)\frac{df}{dt}+v\mu\hat{e}_b\cdot\nabla F + \frac{(1-\mu^2)}{2}\left[v\hat{e}_b\cdot\nabla\ln B-\frac{2}{v}\hat{e}_b\cdot\frac{d\mathbf{V}}{dt}+\mu\frac{d\ln\left(nr/B^3\right)}{dt}\right]\frac{\partial f}{\partial\mu} + \left[-\frac{\mu\hat{e}_b}{v}\cdot\frac{d\mathbf{V}}{dt}+\mu^2\frac{d\ln(n/B)}{dt}+\frac{1-\mu^2}{2}\frac{d\ln B}{dt}\right]\frac{\partial f}{\partial\ln p} = \frac{\partial}{\partial\mu}\left(\frac{D_{\mu\mu}}{2}\frac{\partial f}{\partial\mu}\right)-\frac{1}{p^2}\frac{\partial}{\partial p}\left(p^2D_{pp}\frac{\partial f_0}{\partial p}\right). \quad (1)$$

Here $\hat{e}_b$ is the unit vector along the magnetic field, μ is the cosine of the pitch angle, n is the solar wind density, B is the magnetic field strength, p is the ion momentum, the pitch angle diffusion coefficient is given by

$$D_{\mu\mu}=\left(\frac{R_1}{r}\right)^{3/2}\frac{(1-\mu^2)v}{2\lambda_0}, \quad (2)$$

where the parallel mean free path at R_1 = 1 AU is λ_0, and the coefficient associated with diffusion of particle speed (or equivalently, momentum) is

$$\frac{D_{pp}}{p^2}=\eta^2D_0v/V. \quad (3)$$

Here, the ensemble averaged square of the longitudinal field variations is $\eta^2 = \langle(B - B_0)^2/B_0^2\rangle$, where B_0 is the mean magnetic field. The coefficient D_0 characterizes the rate of stochastic acceleration. For reference, an average value of η^2 = 0.05 is characteristic of the variations observed by Ulysses out near 4 AU in slow solar wind. This form for stochastic acceleration term was derived by *Schwadron et al.* [1996] based on Ulysses observations of interplanetary acceleration of pickup protons.

[23] The form of the stochastic acceleration term can be easily modified within the code. In the pickup ion application described here, we take a value of $D_0 = 4 \times 10^{-6}$ s^{-1}. The distribution function is averaged over gyrophase and is a function of time, position, particle momentum, and pitch angle: $f = f(t, \mathbf{x}, p, \mu)$.

[24] The formulation of the pitch angle diffusion coefficient is also highly flexible. The expression for the pitch angle scattering term (2) is based on previous applications; however, in the future when coupled to MHD solutions, it may become convenient to express the mean free path as a function of the plasma density. For example, if the diffusion coefficient scales with the plasma density, the scattering mean free path will become smaller near enhanced density structures such as foreshocks.

[25] The advantage of the focused transport formulation in (1) is that coefficients are expressed as time derivatives in the frame of reference moving with the plasma. Therefore, in the system of nodes that move with the plasma in EPREM (Figure 4), most of the focused transport coefficients are obtained simply by differencing the state quantities (e.g., density, field strength, plasma velocity) at each node between the updated values (at time t) and the values at the previous time step (at time $t - \Delta t$). Since node lists follow field lines, the field line gradients needed in the second term of (1) are easily computed. This leaves the pitch angle and energy diffusion to be solved as a matrix inversion.

[26] Cross-field diffusion and drift are also solved for within EPREM. At each time step and at each node, we update the distribution based on equation (1). The isotropic portion of the distribution function is formed from the average of the distribution over pitch angle, $f_0(t, \mathbf{x}, p) = 1/2\int_{-1}^{1}d\mu f(t, \mathbf{x}, p, \mu)$ and is then updated at each time step in a separate routine according to the following convection-diffusion equation [*Jokipii et al.*, 1977; *Lee and Fisk*, 1981]:

$$\frac{\partial f_0}{\partial t}=\nabla\cdot\left(\boldsymbol{\kappa}_\perp\cdot\nabla f_0\right)-\mathbf{v}_D\cdot\nabla f_0=0, \quad (4)$$

where

$$\mathbf{v}_D=\frac{cvp}{3q}\nabla\times\left(\frac{\mathbf{B}}{B^2}\right). \quad (5)$$

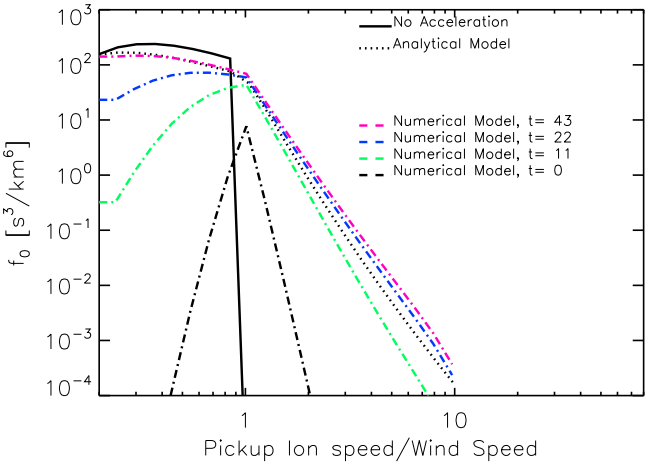

Figure 5. Comparison between results from the EPREM code (f_0 is the isotropic part of the distribution function calculated by the model) and the analytic models of *Vasyliunas and Siscoe* [1976], which neglects stochastic acceleration (solid curve), and *Schwadron et al.* [1996], which includes stochastic acceleration. Pickup ions are included through a source term that injects a pickup ion ring distribution. Time steps are ~10 min, and it requires about 30 time steps to converge to a solution.

Note that diffusion has been neglected from (4) since it is already solved for in the focused transport equation (1). In both the case of drift and perpendicular diffusion we use an explicit differencing method applied to the node shells. We identify the North, East, West and South nearest neighbors of each node. We then find the gradients associated with the nearest neighbor differences applied to the isotropic distribution. The gradients are then projected perpendicular to the field to determine the diffusion term. The drift term is solved as the dot product of the drift velocity with the gradient operator based on nearest neighbor differences of the isotropic distribution function. In this case, it is relatively straightforward to solve this gradient operator to second order. The drift velocity is solved assuming that the local structure of the field is functionally similar to the Parker spiral. The ratio of the azimuthal field to the radial field, the field strength, and polarity are used to solve for the local structure of the field (making no assumption about distance from the Sun). The curl is then applied using the functional form of the Parker magnetic spiral, and the drift velocity is solved analytically. This avoids numerical difficulties in computing the curl operator, but approximates the drift according to a Parker spiral field structure, which has no azimuthal velocity component. In practice, even with large transient disturbances, the spiral structure is largely retained (becoming overwound or underwound depending on whether the local field is compressed or rarefied) and the drift velocity calculated using this technique retains the main features of the curvature and gradient drift.

[27] The energetic particle solver is broken up into five separate steps, in which we solve the change to the distribution function at each node due to (1) adiabatic change (the term involving $\partial f/\partial \ln p$ in (1)), (2) diffusive streaming (the $v\mu\hat{e}_b \cdot \nabla f$ and $\partial/\partial\mu\{[D_{\mu\mu}/2]\partial f/\partial\mu\}$ and the adiabatic focusing terms involving the $\partial f/\partial\mu$ operator), (3) shell diffusion (perpendicular diffusion), (4) drift (curl and gradient drift), and (5) diffusive acceleration (involving the $\{1/p^2\}\partial/\partial p\{p^2 D_{pp}\partial f_0/\partial p\}$). There is a single macro−time step in which all sub−time steps are applied and the energetic particle solution for the distribution function at each node is advanced. In each of the sub−time steps, we solve for the time change needed to maintain numerical stability and then advance by a series of these smaller sub−time steps to achieve the macro−time step. The macro−time step must be small enough so that the individual substeps remain tightly coupled. In the runs described in this paper, we have used macro−time steps on the order of tens of seconds, and the sub−time steps can be as small as 1 s intervals. The smallest sub−time steps are regulated by diffusive streaming at the highest levels in the energy grid. In practice, we apply the criterion that the sub−time steps cannot be more than an order of magnitude smaller than the macro−time steps, insuring the substeps remain tightly coupled.

[28] The energetic particle solvers have been developed to work robustly over a wide range of energies. As such, we have applied the code for both relatively low energy pickup ions (500 eV to 10 keV) and much higher energy solar energetic particle events (1 MeV to 1 GeV). For example, *Hill et al.* [2009] applied EPREM to study the evolution of pickup He^+ and suprathermal solar wind He^{++} as a function of distance from the Sun. In this application we used a lower-energy boundary near 500 eV/nucleon, which is substantially lower than the injection energy of pickup ions. The pickup ions were injected as a ring distribution. We took an upper energy boundary at 100 keV and an energy grid composed of 100 logarithmically spaced steps. The solar wind alphas were assumed to adopt the form of the kappa distribution beneath the energy boundary. The two lowest-energy steps near 500 eV were then updated with appropriate values from the kappa function at each time step. We validated our solution method at low energies by comparing numerical to analytic solutions.

[29] An example of a validation run is shown in Figure 5 for pickup He^+. We show 4 time steps as the code converges to a solution. The solution is compared to two analytic functions: the *Vasyliunas and Siscoe* [1976] solution (solid curve); and the analytic solution of *Schwadron et al.* [1996]. These solutions were taken at 4 AU with identical values for the neutral interstellar densities (0.01 cm^{-3}), spatial distribution (we use an $\exp(-l/r)$ spatial distribution with l = 1 AU), production rate (3.5×10^{-7} s^{-1} at 1 AU), and stochastic acceleration rate as given above. It can be seen that the numerical model converges, and slightly

exceeds the analytic model at higher energies. This slight excess is not a numerical error. The numerical model includes terms that are neglected in the analytic model. Most importantly, the numerical model includes pitch angle diffusion with a scattering mean free path of 1 AU, and therefore diffusive streaming of pickup ions. There is an outward gradient in the pickup ions, which causes a slight excess in the distribution at higher energies where the pickup ions have higher mobility and stream in from beyond 4 AU. Overall, the agreement between the analytic model and the numerical model is excellent.

[30] The validation run in Figure 5 is one example of a number of validation runs that have been performed. We have also built the code so that modules for updating the energetic particles can be interchanged easily. As such, the code itself will likely be updated and improved continually.

[31] The EPREM code was designed for a wide array of energetic particle applications using a range of energies from suprathermal ions, pickup ions, low-energy energetic particles and up to GeV cosmic rays. This flexibility is afforded by the application of robust solvers applied in the comoving reference frame, and the ability to modify the energy range, step size, and the application of boundary conditions in energy space.

2.3. EMMREM Baryon Transport Module

[32] The EMMREM specific version of the BRYNTRN code (Looping BRYNTRN [*Wilson et al.*, 1991]) is a FORTRAN code driven by a parallelized Perl script, which loops over a series of snapshots of the proton differential flux at different steps in a time series. The code is capable of performing near real-time simulations of SEPs that provide organ doses and dose equivalents, using computerized anatomical models of the shielding of radio-sensitive organs, for thinly shielded spacecraft. The code has been used for various studies involving several large historical SEP events.

[33] The interface for the BRYNTRN code enables it to accept input from the EPREM module. The user-supplied input mode of BRYNTRN was identified as the method of choice and an interface shell developed at UT to enable a seamless input into the transport module [*Hatcher et al.*, 2009].

[34] A 3-layer version of BRYNTRN that incorporates Mars atmosphere shielding effects has been configured to calculate dose and dose equivalent for Martian surface and atmosphere scenarios (L. Townsend et al., Transmission of solar energetic particles and galactic cosmic rays through the Mars atmosphere, manuscript in preparation, 2009). Fluence or flux distributions will be considered in the future. The code has been used to develop a lookup table of effective dose, organ doses and dose equivalents behind thicknesses of aluminum shielding relevant to habitat or surface rover configurations anywhere on the Martian surface. A lookup table is required because the SEP protons must be transported through as much as 500 g/cm^2 of shield materials. Calculations at such depths cannot be carried out in near real time simulations. A BRYNTRN version has also been configured to calculate dose in Silicon for comparison with future dosimeter measurements anywhere on the surface of Mars.

2.4. Galactic Cosmic Ray Doses

[35] A 3-layer version of HZETRN 2005 that incorporates Mars atmosphere shielding effects has been configured to calculate GCR dose and dose equivalent for Martian surface and atmosphere scenarios (Townsend et al., manuscript in preparation, 2009). The code has been used to develop a lookup table of daily effective dose, organ doses and dose equivalents behind thicknesses of aluminum shielding relevant to habitat or surface rover configurations anywhere on the Martian surface. The Badhwar-O'Neill GCR model for interplanetary magnetic field potentials ranging from the most highly probable solar minimum (450 MV) to solar maximum conditions (1800 MV) in the solar cycle is used as input into the calculations. This model is the standard one used for space operations at the Space Radiation Analysis Group (SRAG) at NASA Johnson Space Center. A lookup table is used because the large spread in interplanetary magnetic field conditions, large numbers of GCR ion species and their many reaction product secondary particles must be transported through as much as 500 g/cm^2 of shield materials. Calculations of such complex spectra at such depths take approximately half a day for each possible spectrum and cannot be carried out in near real time simulations. Also, since GCR intensities change very little from day to day, daily dose and dose equivalent estimates are sufficient and are consistent with the typical time frames for SEP event exposures, thereby enabling relative comparisons to be made between them. In addition, the HZETRN 2005 code itself is export controlled, which precludes it from being publicly available, although its use to generate dose data for this project is approved and licensed by NASA Langley Research Center. HZETRN 2005 was selected for use in the project, over earlier, publicly released versions of HZETRN, because it is the most up to date and complete version available.

[36] Figure 6 shows an example of the calculation of dose rate from GCRs. We show here the dose rates in 1 g/cm^2 of water (Figure 6, top) and 10 g/cm^2 of water (Figure 6, bottom), which are used as proxies for skin doses and blood forming organ (BFO) doses, respectively, behind various thicknesses of Al. The Al thicknesses serve as proxies for shielding of a nominal spacesuit (0.3 g/cm^2), a thick spacesuit (1 g/c^2), nominal spacecraft shielding (5 g/cm^2) and thick spacecraft shielding (a storm shield; 10 g/cm^2). More detailed organ doses have also been solved for using HZETRN 2005 and are detailed by Townsend et al. (manuscript in preparation, 2009).

[37] The GCR dose rates are shown as a function of the modulation potential, which is the approximate energy loss of a galactic cosmic ray on its entry through the heliosphere. The modulation potential varies with the solar cycle. During solar maximum, larger interplanetary field

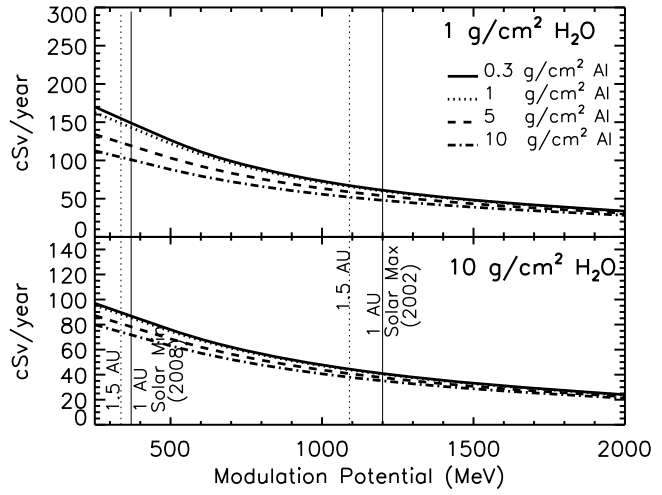

Figure 6. Dose rates of galactic cosmic rays (GCRs) through various thicknesses of Al and water. The Al thicknesses serve as proxies for a nominal spacesuit thickness (0.3 g/cm^2), a thick spacesuit (1 g/cm^2), nominal spacecraft shielding (5 g/cm^2), and thick spacecraft shielding (a storm shelter, 10 g/cm^2). The water thicknesses serve as proxies for (top) skin doses (1 g/cm^2) and (bottom) blood forming organ (BFO) doses (10 g/cm^2). The GCR intensity is characterized as a function of the modulation potential, defined as the energy loss of GCRs from the outer modulation boundary [*Badhwar and O'Neill*, 1994]. The incident spectrum at the modulation boundary is from *O'Neill* [2006]. We also show the modulation potential from the most recent solar minimum and solar maximum (vertical lines) at 1 AU (solid lines) and 1.5 AU (dashed lines).

strengths and the presence of closed magnetic flux from coronal mass ejections [*Schwadron et al.*, 2008] causes stronger GCR modulation and decreases the flux of GCRs in the inner solar system (e.g., near the Earth, Moon and Mars). Therefore the modulation potential is larger near solar maximum. We show as vertical solid lines in Figure 6 the modulation potential derived from neutron fluxes at Earth [*O'Neill*, 2006] near solar minimum in 2008 and near solar maximum in 2002. The modulation potential is derived from the modulation parameter,

$$\phi(r) = \int_r^{R_b} \frac{V(x)}{3\kappa_1(x)} dx, \tag{6}$$

where the modulation potential is $\Phi = |Ze|\phi(r)$, the integral extends from the inner boundary at radius r to the outer modulation boundary R_b, the solar wind speed is $V(x)$ and $\kappa_1(x)$ is related to the radial diffusion coefficient, κ. In particular, the form for κ is based on a fit to the observed spectrum over time and species [*O'Neill*, 2006]: $\kappa = \kappa_1(r)P\beta$ where P is the rigidity in GV, β is the particle speed over the speed of light, $\kappa_1(r) \propto 1+(r/r_0)^2$ and $r_0 = 4$ AU. Equation (6) is solved explicitly so that the modulation potential at a given radial distance at time, $\Phi(r, t)$, can be determined from the modulation potential inferred at $r_1 = 1$ AU, $\Phi_1(t)$:

$$\Phi(r,t) = \Phi_1\left(\frac{\arctan(R_b/r_0) - \arctan(r/r_0)}{\arctan(R_b/r_0) - \arctan(r_1/r_0)}\right). \tag{7}$$

The vertical dashed lines then show the modulation potential near Mars (at 1.5 AU) during the periods near solar max and min. The modulation potential near Mars is only slightly lower than that near 1 AU.

[38] The doses derived in Figure 6 are substantial compared to the career effective dose limits for 1 year missions [*NASA*, 2007, Table 3]. For example, a 40 year old male and female have a career dose limits for a 1 year mission of 80 cSv and 62 cSv, respectively. However, the use of proxies generally can lead to an overestimate of expected doses. Nevertheless, GCRs represent a significant issue for long-term exposure to the space environment.

3. Examples of EMMREM Event Runs

[39] Although the studies of pickup ions and suprathermal ions at low energies have helped substantially in the development of EPREM, the applications that are most critical to the EMMREM project treat much higher energy ions (1 MeV to 1 GeV). We have developed interfaces to the secondary transport modules and lookup tables that allow us to compute doses and dose rates from essentially any model or observational data set that generates distribution functions and time series. For example, an interface to the PATH code [*Verkhoglyadova et al.*, 2009] is currently in work (G. Zank et al., Modeling gradual solar energetic particle and energetic storm particle events using the physics based model PATH, manuscript in preparation, 2009).

[40] We have developed the functionality in EPREM to read data from GOES, ACE and other spacecraft and then project energetic particles into the inner heliosphere. We are pursuing the concept that operating spacecraft that observe energetic particles will allow us to assess the evolution of the radiation environment both near the spacecraft and throughout the near ecliptic regions of the inner heliosphere. The difficulty with this approach is that spacecraft observe energetic particles only at a single location. It is necessary to make some approximation to project the information from the one longitude (e.g., at geostationary orbit in the case of GOES) to all longitudes near 1 AU. We have attempted a number of approaches to the problem, but the simplest approach of projecting the time series observed at GEO to all longitudes is a sensible starting point. The Compton-Getting effect raises a small complication in transforming the differential intensity from the spacecraft reference frame into the natural frame of energetic particles, which comoves with the solar wind. At relatively high energies

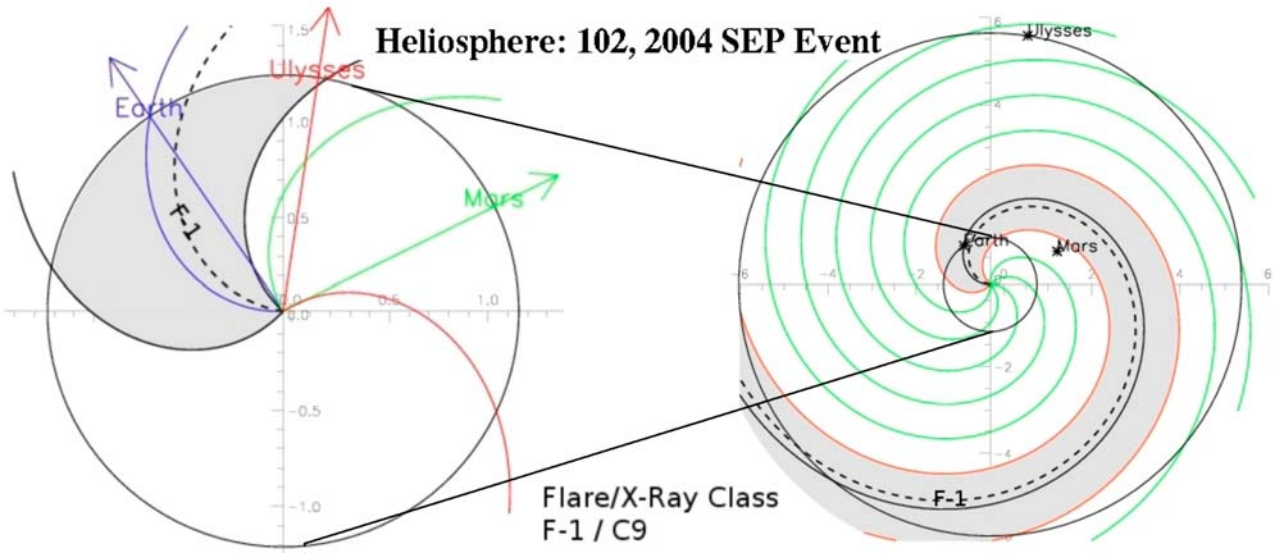

Figure 7. The configuration of an SEP on day 102 (12 April) of 2004. (left) The location of a flare (dashed line), the Earth connected field line (blue), the Mars connected field line (green), and the Ulysses connected field line (red). The shaded region shows a reference range of longitudes within 45° of the flare line. The vectors show the directions to the three observers. (right) The overall field configuration out to Ulysses.

(> MeV), this introduces only a small correction because the particle speed is so much larger than the solar wind speed.

[41] Figure 7 shows the field configuration, the alignment of the flare, and the configuration of the observers near the time of a relatively isolated flare that occurred on 12 April 2004. Ulysses in this case was on field lines almost 180° off in longitude from the flare site and from the Earth connected field line. Nevertheless, we see in Figure 8 (right) that Ulysses observed this event. In fact, the simulation does a decent job of reproducing the data at Ulysses, particularly at the onset of the event and the peak intensities at different energies. The simulations do not include anomalous cosmic rays and galactic cosmic rays. This

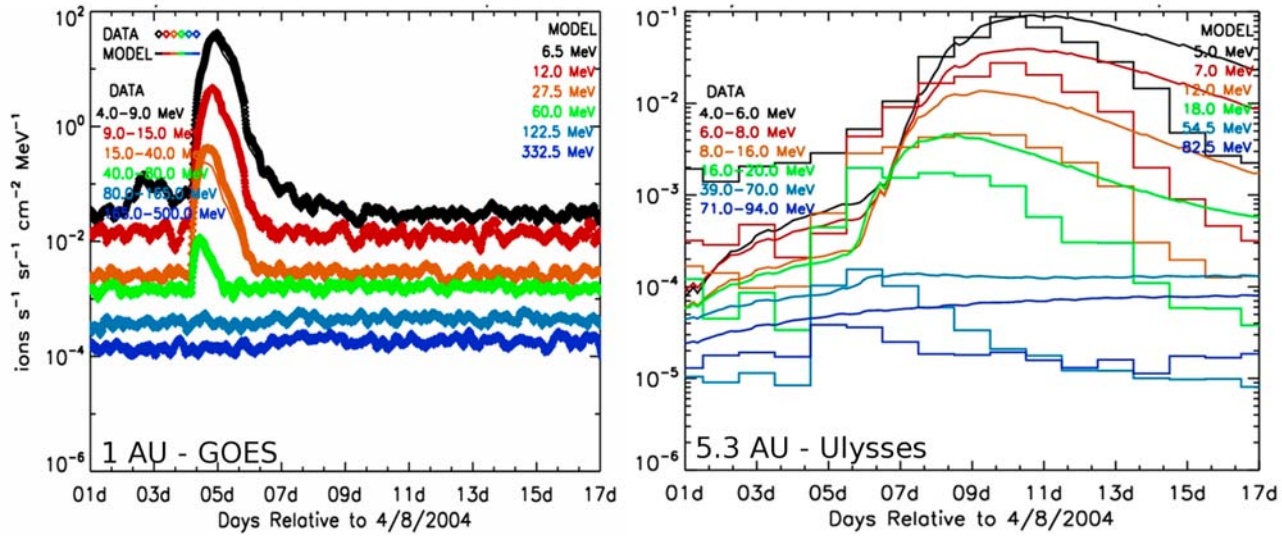

Figure 8. (left) The 1 AU observed fluxes and (right) the particle fluxes integrated out to Ulysses along with the observed daily averaged PHA fluxes. In this event the Ulysses-connected field line is almost 180° off of the Earth-connected field line and from the flare. Nevertheless, the event onset and integrated fluxes are comparable.

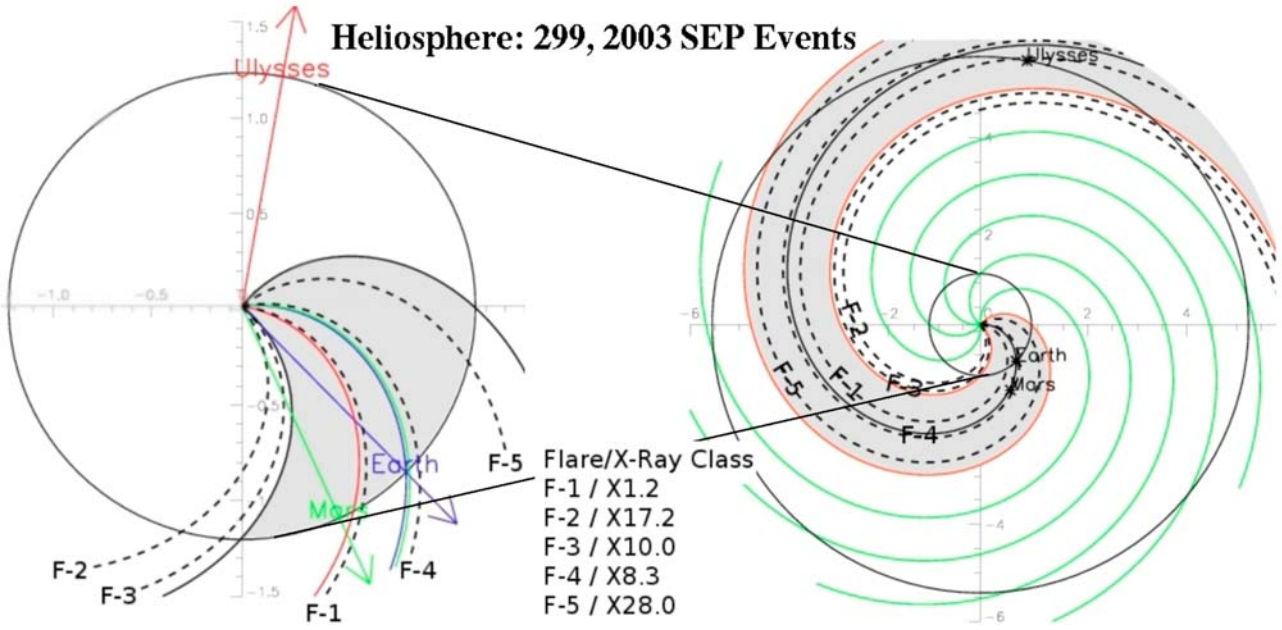

Figure 9. The configuration of October 2003 SEP events (the Halloween storms). (left) The location of the largest 5 flares (dashed lines) associated with this series of events [*Lario et al.*, 2005], the Earth connected field line (blue), the Mars connected field line (green), and the Ulysses connected field line (red). *Lario et al.* [2005] studied these events in detail, and there were 10 shocks observed at ACE and 5 coronal mass ejections. The shaded region shows a reference range of longitudes within 45° of the first flare line (magnetically aligned with Earth). The vectors show the directions to the three observers. (right) The overall field configuration out to Ulysses. In this case, Ulysses, Mars, and Earth are fairly well aligned.

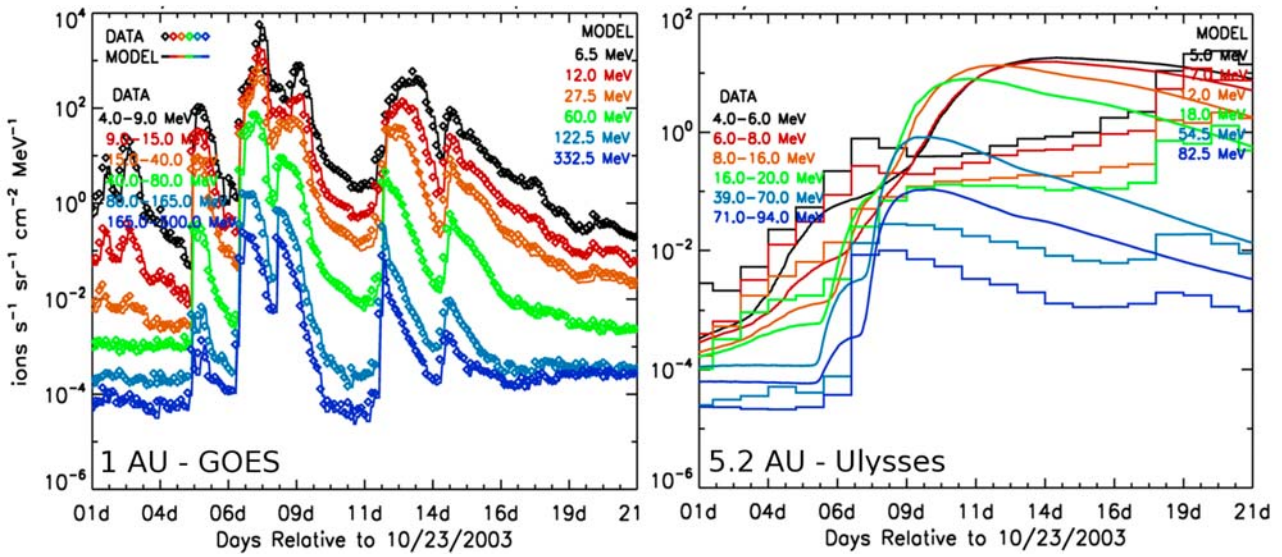

Figure 10. (left) The 1 AU observed fluxes and (right) the particle fluxes integrated out to Ulysses overplotted with the observed daily averaged PHA fluxes. In this complex event, the Ulysses-connected field line is about 20° off of the Earth-connected field line. Nevertheless, the event onset and integrated fluxes are comparable to those observed by Ulysses.

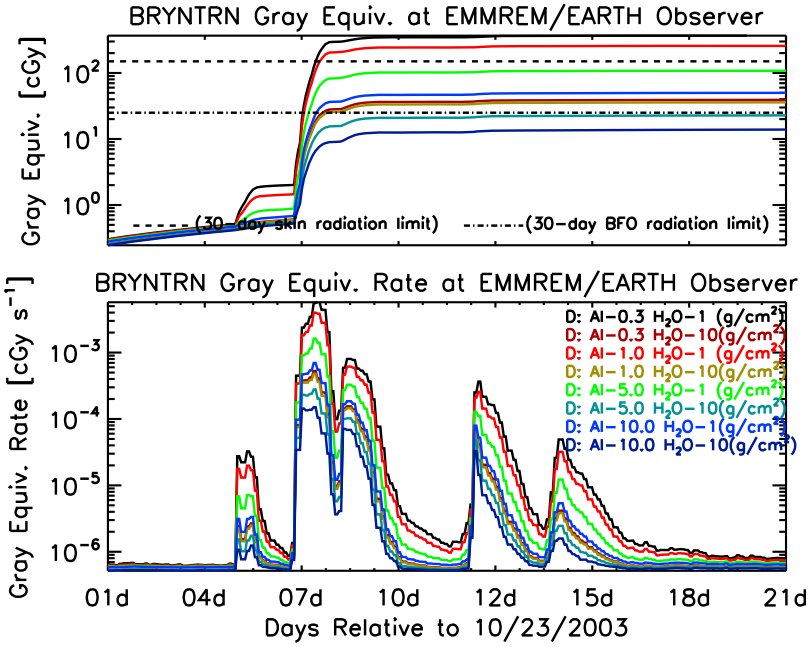

Figure 11. (top) Accumulated doses and (bottom) gray equivalent dose rates near Earth during the 2003 Halloween events. We show proxies for skin/eye dose (1 g/cm^2 H_2O) and doses in BFO (10 g/cm^2 H_2O) behind 0.3, 1, 5, and 10 g/cm^2 of shielding. The skin dose exceeds the 30 day limits as stated by *NASA* [2007] for shielding thicknesses up to 5 g/cm^2.

makes it somewhat difficult to compare the data and model at higher energies, considering that this is not a large SEP event (Class C flare).

[42] There is an important detail in the simulation concerning the assumed scattering mean free path, which greatly affects the propagation and evolution of the event to Ulysses. We have assumed that the parallel scattering mean free path is proportional to particle rigidity to the 1/3 power and scale the mean free path by a nominal value at 1 GV rigidity. We have found that a 1 GV mean free path of 0.05 AU does a reasonable job with the event onsets at each of the observers (M. A. Dayeh et al., Proton intensity gradients and radiation dose equivalents in the inner heliosphere: Modeling and prediction, manuscript in preparation, 2009). The form we have assumed for the scattering mean free path is appropriate for the observed spectrum of background magnetohydrodynamic turbulence [e.g., *Shalchi et al.*, 2006]; however, the scattering mean free path needed is fairly small, suggesting that the flare particles may be creating wave enhancements that reduce the mean free path. A more self-consistent wave-particle theory would likely improve the propagation model.

[43] A second much larger event, the Halloween storms of 2003, is shown in Figures 9 and 10. In this case, the field lines connected to the Earth, Ulysses and Mars are fairly well aligned. The modeled and observed data show general correlation, however the model over predicts the fluxes are Ulysses observed during the event.

[44] An example of the BRYNTRN dose rates (Figure 11, bottom) and accumulated doses (Figure 11, top) are shown for the near Earth space environment during the Halloween storms of 2003. In both cases we find that the skin doses exceed the 30 day limits (dashed horizontal line [*NASA*, 2007]) for Al shielding thicknesses less than 5 g/cm^2,

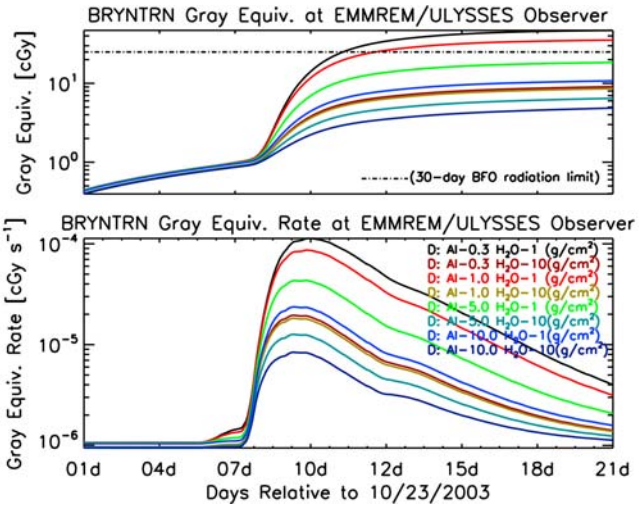

Figure 12. (top) Accumulated doses and (bottom) gray equivalent dose rates at Ulysses during the 2003 Halloween events as predicted from fluxes propagated out from 1 AU by EPREM. We show the same proxies for the skin/eye and BFO doses as in Figure 11.

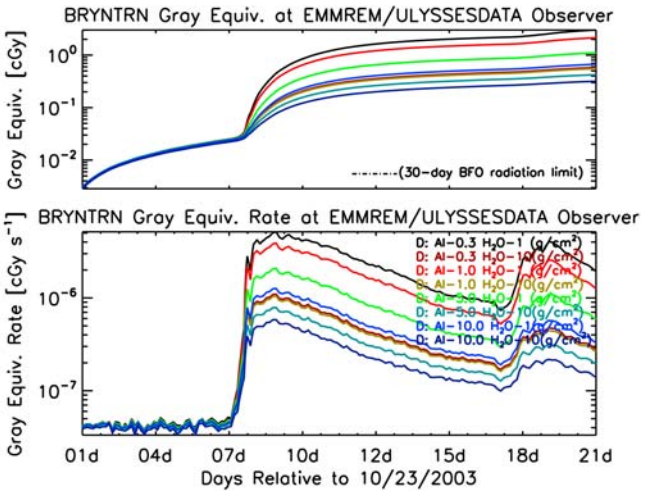

Figure 13. (top) Accumulated doses and (bottom) gray equivalent dose rates near Ulysses during the 2003 Halloween events as predicted from measured energetic particle fluxes. The accumulated doses and dose rates early on in the event are almost a decade below the levels predicted by the model.

however the BFO doses never exceed the 30 day limits (dash-dotted horizontal line).

[45] The validation at Ulysses for the 2003 event shows some extremely interesting trends. The flux comparison in Figure 10 suggests that the model was capturing many of the observed trends. However, Figures 12 and 13 show the doses derived from EPREM predictions and those derived from observed fluxes at Ulysses. The fluxes modeled by EPREM lead to an over estimate in the predicted doses by about an order of magnitude.

4. Summary

[46] We have described the Earth-Moon-Mars Radiation Environment Module (EMMREM), which provides the heliophysics and radiation biology communities with the capability to run solar energetic particle event time series based on observations near Earth or simulated through the inner heliosphere and to specify the impacts of the radiation environment in terms of time-dependent dose-related quantities. EMMREM has already made the critical step of connecting secondary transport codes with observed or simulated time series of solar energetic particles and cosmic rays. This enables a number of important advances including the development of a forecasting tool (A. Posner et al., A path towards the first prompt-SEP dose-rate forecasting for the Earth-Moon system: Coupling RELEASE and EMMREM, manuscript in preparation, 2009), the application of secondary transport through Mars atmosphere (Townsend et al., manuscript in preparation, 2009), the development of risk metrics associated with event scenarios (F. A. Cucinotta et al., Overview of risk assessment approaches for solar particle events, manuscript in preparation, 2009), and the integration of radiation biology secondary transport codes with sophisticated simulations of gradual energetic particle events (Zank et al., manuscript in preparation, 2009).

[47] We have shown a number of examples of the EMMREM capabilities. Measurements of energetic particles near 1 AU can be ingested into the Energetic Particle Radiation Environment Module (EPREM) and projected to various locations throughout the inner heliosphere. This capability was used to compare the evolution of events near Earth and at the Ulysses spacecraft. The comparison was made for two events in April 2004 and the Halloween storms (October and November) of 2003. Generally, the simulated and observed time series at Ulysses compare quite well to the model predictions. This is somewhat remarkable given that the Ulysses-connected magnetic field line is almost 180° from the near-Earth field line in the April 2004 event.

[48] Near the beginning of the 2003 Halloween storms, the predictions from the model overestimate the observed flux, while successfully describing the event onsets. It is possible that solar energetic particles were suppressed by magnetic and compressive barriers convected with the solar wind [*Lario et al.*, 2005, 2008]. The simulations used in this paper were run with a uniform radial solar wind; therefore magnetic and compressive barriers were neglected. The concept that such structures reduce the energetic particle flux at radial distances beyond 1 AU is further investigated by including the predictions of solar wind MHD models, which simulate compression regions and MHD boundaries, in the EPREM solutions (Kozarev et al., manuscript in preparation, 2009).

[49] The accumulated doses and dose rates from the 2003 Halloween storms were derived from the looping version of BRYNTRN model used in EMMREM. The results show that the proxies for Skin/Eye doses (1 g/cm^2 of H_2O) and BFO doses (10 g/cm^2 of H_2O) exceed 30 day radiation limits for Al shielding material less than 1 g/cm^2, which is indicative of spacesuit shielding. The accumulation of these doses occurred over a period of about a half of a day. Therefore, this event was quite dangerous, but much of the hazard could have been mitigated if astronauts had sufficient advance warning time and could get behind the thicker shielding provided by a nominal spacecraft.

[50] Thus, we have introduced the Earth-Moon-Mars Radiation Environment Module (EMMREM) project. Existing and extended capabilities of the module will be made available online at Boston University and at the Community Coordinated Modeling Center. The capabilities will enable a greater understanding of the radiation environment, help to guide the development of more useful predictive space weather tools, and the development of appropriate shielding materials for human missions to the Moon and beyond.

[51] **Acknowledgments.** Research support from the NASA LWS EMMREM project and grant NNX07AC14G is gratefully acknowledged.

References

Badhwar, G. D., and P. M. O'Neill (1994), Long-term modulation of galactic cosmic radiation and its model for space exploration, *Adv. Space Res.*, *14*(10), 749.

Cucinotta, F. A. (1999), Issues in risk assessment from solar particle events, *Radiat. Meas.*, *30*, 261.

Cucinotta, F. A., J. W. Wilson, J. R. Williams, and J. F. Dicello (2000), Analysis of MIR-18 results for physical and biological dosimetry: Radiation shielding effectiveness in LEO, *Radiat. Meas.*, *132*, 181.

Cucinotta, F. A., W. Schimmerling, J. W. Wilson, L. E. Peterson, G. D. Badhwar, P. B. Saganti, and J. F. Dicello (2001), Space radiation cancer risks and uncertainties for Mars missions, *Radiat. Res.*, *156*, 682.

Domingo, V., B. Fleck, and A. I. Poland (1995), The SOHO mission: An overview, *Sol. Phys.*, *162*, 1.

George, K., V. Willingham, H. Wu, D. Gridley, G. Nelson, and F. A. Cucinotta (2002), Chromosome aberrations in human lymphocytes induced by 250 MeV protons: Effects of dose, dose rate and shielding, *Adv. Space Res.*, *30*(4), 891.

Hatcher, R., L. W. Townsend, N. A. Schwadron, and K. Kozarev (2009), Status of developing a near real-time capability for estimating space radiation exposure using EMMREM, paper SAE 2009-01-2340 presented at 39th International Conference on Environmental Systems, SAE Int., Savannah, Ga., 12–16 July.

Hill, M. E., N. A. Schwadron, D. C. Hamilton, R. D. Di Fabio, and R. K. Squier (2009), Interplanetary suprathermal He^{+} and He^{++} observations during quiet periods from 1 to 9 AU and implications for particle acceleration, *Astrophys. J.*, *699*, L26, doi:10.1088/0004-637X/699/1/L26.

Jokipii, J. R., E. H. Levy, and W. B. Hubbard (1977), Effects of particle drift on cosmic-ray transport. I: General properties, application to solar modulation, *Astrophys. J.*, *213*, 861.

Kóta, J., W. B. Manchester, and T. I. Gombosi (2005), SEP acceleration at realistic CMEs: Two sites of acceleration?, in *Proceedings of the 29th International Cosmic Ray Conference*, vol. *1*, edited by B. Sripathi Acharya et al., p. 125, Tate Inst. of Fundam. Res., Mumbai, India.

Lario, D., R. B. Decker, S. Livi, S. M. Krimigis, E. C. Roelof, C. T. Russell, and C. D. Fry (2005), Heliospheric energetic particle observations during the October–November 2003 events, *J. Geophys. Res.*, *110*, A09S11, doi:10.1029/2004JA010940.

Lario, D., R. B. Decker, O. E. Malandraki, and L. J. Lanzerotti (2008), Influence of large-scale interplanetary structures on energetic particle propagation: September 2004 event at Ulysses and ACE, *J. Geophys. Res.*, *113*, A03105, doi:10.1029/2007JA012721.

Lee, M. A., and L. A. Fisk (1981), The role of particle drifts in solar modulation, *Astrophys. J.*, *248*, 836.

Le Roux, J. A., and M. S. Potgieter (1995), The simulation of complete 11 and 12 year modulation cycles for cosmic rays in the heliosphere using a drift model with global merged interaction regions, *Astrophys. J.*, *442*, 847, doi:10.1086/175487.

NASA (2007), NASA Space Flight Human System Standard, vol. 1, Crew Health, *Rep. NASA-STD-3001*, Washington, D. C.

Ng, C. K., D. V. Reames, and A. J. Tylka (2003), Modeling shock-accelerated solar energetic particles coupled to interplanetary Alfvén waves, *Astrophys. J.*, *591*, 461, doi:10.1086/375293.

Nikjoo, H., I. K. Khvostunov, and F. A. Cucinotta (2002), The response of tissue-equivalent proportional counters to heavy ions, *Radiat. Res.*, *157*, 435.

O'Neill, P. M. (2006), Badhwar-O'Neill galactic cosmic ray model update based on Advanced Composition Explorer (ACE) energy spectra from 1997 to present, *Adv. Space Res.*, *37*(9), 1727.

Owens, M. J., and N. U. Crooker (2006), Coronal mass ejections and magnetic flux buildup in the heliosphere, *J. Geophys. Res.*, *111*, A10104, doi:10.1029/2006JA011641.

Potgieter, M. S., R. A. Burger, and S. E. S. Ferreira (2001), Modulation of cosmic rays in the heliosphere from solar minimum to maximum: A theoretical perspective, *Space Sci. Rev.*, *97*, 295, 10.1023/A:1011837303094.

Ruffolo, D. (1995), Effect of adiabatic deceleration on the focused transport of solar cosmic rays, *Astrophys. J.*, *442*, 861.

Sauer, H. H. (1993), GOES observations of energetic protons e > 685 MeV: Description and data comparison, in *23rd International Cosmic Ray Conference*, vol. *3*, edited by D. A. Leahy, R. B. Hicks, and D. Venkatesan, p. 250, World Sci., Singapore.

Saunders, R. S., et al. (2001), 2001 Mars Odyssey mission summary, *Space Sci. Rev.*, *110*, 1.

Schwadron, N. A., L. A. Fisk, and G. Gloeckler (1996), Statisitical acceleration of interstellar pick-up ions in co-rotating interaction regions, *Geophys. Res. Lett.*, *23*, 2871.

Schwadron, N. A., M. Owens, and N. U. Crooker (2008), The heliospheric magnetic field over the Hale cycle, *Astrophys. Space Sci. Trans.*, *4*, 19.

Shalchi, A., J. W. Bieber, W. H. Matthaeus, and R. Schlickeiser (2006), Parallel and perpendicular transport of heliospheric cosmic rays in an improved dynamical turbulence model, *Astrophys. J.*, *642*, 230.

Skilling, J. (1971), Cosmic rays in the galaxy: Convection or diffusion?, *Astrophys. J.*, *170*, 265.

Stone, E. C., A. M. Frandsen, R. A. Mewaldt, E. R. Christian, D. Margolies, J. F. Ormes, and F. Snow (1998), The Advanced Composition Explorer, *Space Sci. Rev.*, *86*, 1, doi:10.1023/A:1005082526237.

Torsti, J., et al. (1995), Energetic particle experiment ERNE, *Sol. Phys.*, *162*, 505, doi:10.1007/BF00733438.

Tylka, A. J. (2001), New insights on solar energetic particles from Wind and ACE, *J. Geophys. Res.*, *106*, 25333, doi:10.1029/2000JA004028.

Vasyliunas, V. M., and G. L. Siscoe (1976), On the flux and the energy spectrum of interstellar ions in the solar system, *J. Geophys. Res.*, *81*, 1247.

Verkhoglyadova, O. P., G. Li, G. P. Zank, Q. Hu, and R. A. Mewaldt (2009), Using the PATH code for modeling gradual SEP events in the inner heliosphere, *Astrophys. J.*, *693*, 894.

Wenzel, K. P., R. G. Marsden, D. E. Page, and E. J. Smith (1992), The Ulysses mission, *Astron. Astrophys. Suppl. Ser.*, *92*, 207.

Wilson, J. W., L. W. Townsend, W. S. Schimmerling, G. S. Khandelwal, F. S. Khan, J. E. Nealy, F. A. Cucinotta, L. C. Simonsen, J. L. Shinn, and J. W. Norbury (1991), Transport methods and interactions for space radiations, *NASA Tech. Rep.*, 1257.

Wilson, J. W., F. A. Cucinotta, J. Miller, J. L. Shinn, S. A. Thibeault, R. C. Singleterry, L. C. Simonsen, and M. H. Kim (1999), Materials for shielding astronauts from the hazards of space radiations, *Mater. Res. Soc. Symp. Proc.*, *551*, 3.

F. Cucinotta and M.-Y. Kim, Johnson Space Center, NASA, 2101 NASA Pkwy., Houston, TX 77058, USA. (francis.a.cucinotta1@jsc.nasa.gov; myung-hee.y.kim1@jsc.nasa.gov)

M. A. Dayeh and M. Desai, Southwest Research Institute, 6220 Culebra Rd., San Antonio, TX 78238-5166, USA. (maldayeh@swri.edu; mdesai@swri.edu)

M. Golightly, K. Kozarev, N. A. Schwadron, and H. Spence, Department of Astronomy, Boston University, 275 Commonwealth Ave., Boston, MA 01760, USA. (kozarev@bu.edu; nathanas@bu.edu)

D. Hassler, Space Studies Department, Southwest Research Institute, 1050 Walnut St., Ste. 300, Boulder, CO 80302, USA.

R. Hatcher, M. PourArsalan, and L. Townsend, Department of Nuclear Engineering, University of Tennessee, 211 Pasqua Nuclear Engineering Bldg., 1004 Estabrook Rd., Knoxville, TN 37996-2300, USA. (mpourars@utk.edu; ltownsen@tennessee.edu)

A. Posner, NASA Headquarters, Washington, DC 20546, USA. (aposner@swri.edu)

R. K. Squier, Computer Science Department, Georgetown University, 240 Reiss Science Bldg., Washington, DC 20057-1232, USA. (squier@cs.georgetown.edu)